

# The metal content of the circumgalactic medium around star-forming galaxies at $z \sim 2.6$ as revealed by the VIMOS Ultra-Deep Survey.

Méndez-Hernández, H.,<sup>1</sup> Cassata, P.<sup>2,3</sup>, Ibar, E.<sup>1</sup>, Amorín, R.<sup>4,5</sup>, Aravena, M.<sup>6</sup>, Bardelli, S.<sup>7</sup>, Cucciati, O.<sup>7</sup>, Garilli, B.<sup>8</sup>, Giavalisco, M.<sup>9</sup>, Guaita, L.<sup>10</sup>, Hathi, N.<sup>11</sup>, Koekemoer, A.<sup>11</sup>, Le Brun, V.<sup>12</sup>, Lemaux, B.C.<sup>13,14</sup>, Maccagni, D.<sup>8</sup>, Ribeiro, B.<sup>12</sup>, Tasca, L.<sup>12</sup>, Tejos, N.<sup>16</sup>, Thomas, R.<sup>17</sup>, Tresse, L.<sup>12</sup>, Vergani, D.<sup>7</sup>, Zamorani, G.<sup>7</sup>, Zucca, E.<sup>7</sup>

(Affiliations can be found after the references)

Received XXXX XX, 2021; accepted XXXX XX, 2022

## ABSTRACT

**Context.** The circumgalactic medium (CGM) is the location where the interplay between large-scale outflows and accretion onto galaxies occurs. Metals in different ionization states flowing between the circumgalactic and intergalactic mediums are affected by large galactic outflows and low-ionization state inflowing gas. Observational studies on their spatial distribution and their relation with galaxy properties may provide important constraints on models of galaxy formation and evolution.

**Aims.** The main goal of this paper is to provide new insights into the spatial distribution of the circumgalactic of star-forming galaxies at  $1.5 < z < 4.5$  star formation activity in the Universe. We also look for possible correlations between the strength of the low- and high-ionization absorption features (LIS and HIS) and stellar mass, star formation rate, effective radius, and azimuthal angle  $\phi$  that defines the location of the absorbing gas relative to the galaxy disk plane.

**Methods.** The CGM has been primarily detected via the absorption features that it produces on the continuum spectrum of bright *background* sources. We select a sample of 238 close pairs from the VIMOS Ultra Deep Survey to examine the spatial distribution of the gas located around star-forming galaxies and generate composite spectra by co-adding spectra of *background* galaxies that provide different sight-lines across the CGM of star-forming galaxies.

**Results.** We detect LIS (C II and Si II) and HIS (Si IV, C IV) up to separations  $\langle b \rangle = 172$  kpc and 146 kpc. Beyond this separation, we do not detect any significant signal of CGM absorption in the *background* composite spectra. Our Ly $\alpha$ , LIS and HIS rest-frame equivalent width  $W_0$  radial profiles are at the upper envelope of the  $W_0$  measurements at lower redshifts, suggesting a potential redshift evolution for the CGM gas content producing these absorptions. We find a correlation between C II and C IV with star formation rate, stellar mass as well as trends with galaxy size estimated by the effective radius and azimuthal angle. Galaxies with high star formation rate ( $\log[\text{SFR}/(\text{M}_\odot \text{yr}^{-1})] > 1.5$ ) and stellar mass ( $\log[\text{M}_\star/\text{M}_\odot] > 10.2$ ) show stronger C IV absorptions compared with those low SFR ( $\log[\text{SFR}/(\text{M}_\odot \text{yr}^{-1})] < 0.9$ ) and low stellar mass ( $\log[\text{M}_\star/\text{M}_\odot] < 9.26$ ). The latter population instead shows stronger C II absorption than their more massive or more star-forming counterparts. We compute the C II / C IV  $W_0$  line ratio that confirms the C II and C IV correlations with impact parameter, stellar mass and star formation rate. We do not find any correlation with  $\phi$  in agreement with other high-redshift studies and in contradiction to what is observed at low-redshift where large-scale outflows along the minor axis forming bipolar outflows are detected.

**Conclusions.** We find that the stronger C IV line absorptions in the outer regions of these star-forming galaxies could be explained by stronger outflows in galaxies with higher star formation rates and stellar masses, capable of projecting the ionized gas up to large distances, and/or by stronger UV ionizing radiation in these galaxies, able to ionize the gas even at large distances. On the other hand, low-mass galaxies show stronger C II absorptions, suggesting larger reservoirs of cold gas that could be explained by a softer radiation field unable to ionize high-ionization state lines or by the galactic fountain scenario where metal-rich gas ejected from previous star-formation episodes fall back to the galaxy. These large reservoirs of cold neutral gas around low-mass galaxies could be funnelled into the galaxies and eventually provide the necessary fuel to sustain star formation activity.

**Key words.** galaxies: evolution – galaxies: high-redshift – galaxies:ISM – galaxies: CGM

## 1. Introduction

The circumgalactic medium (CGM, 10kpc–300 kpc) is the gas reservoir between the interstellar medium (ISM,  $\lesssim 10$  kpc) and the intergalactic medium (IGM,  $\gtrsim 300$  kpc). It is characterized as an active interface where galaxies reprocess their baryonic material. In fact, up to  $\sim 50\%$  of the total baryonic mass is found in the CGM at both, low-redshift ( $z \sim 0.2$ ) (???) and high-redshift (?), thus representing a significant gas reservoir that can, for example, feed the ISM with gas to form new stars (???). Supernovae explosions or strong stellar winds can deposit metals in the surrounding medium, gas that is mixed with pristine gas accreted from the intergalactic medium (IGM; ?????).

Since the first discoveries of circumgalactic gas around star-forming galaxies (???), its study by direct detection of emission has been a challenge (?). The CGM has been primarily detected via the absorption features that it produces on light from *background* sources. In a pioneering study at high-redshift ( $z \gtrsim 1.5$ ), ?? studied the dependence of the absorption strength on the projected angular separation between *foreground* and *background* galaxies (i.e., impact parameter  $b$ ), reporting absorption detection at impact parameters up to 40 kpc and noticed that absorption strength weakens significantly at larger separations. Thanks to their brightness, quasars are typically used as *background* sources to probe the CGM around *foreground* galaxies (???), allowing to identify the signal produced by extremely low column

densities ( $N_{\text{H I}} \simeq 10^{12} \text{ cm}^{-2}$ ), independent of the properties of the targeted galaxy (e.g., luminosity and/or redshift) (??). This technique has been successful to probe the CGM of galaxies up to redshifts  $z \sim 5$  (?) and has led to the discovery that the CGM is gas rich and has a multi-phase nature (??????).

The CGM has been also characterized using the so-called "down-the-barrel technique", that uses the targeted galaxy itself as a *background* source. Absorption lines redshifted with respect to the galaxy rest-frame evidence the presence of gas flowing towards the galaxy. This result has been interpreted as a strong indication of inflowing material onto the host galaxy (???), while outflows have been identified as blueshifted absorptions in galaxy spectra (??). Although the location of the gas producing the detected absorption is unconstrained, this technique has been successful in studying galactic inflows and outflows from the spectroscopy of star-forming galaxies up to  $z \sim 2 - 3$  (????).

Recently three more techniques have been used to explore the CGM. The first one takes advantage of strong gravitational lensing, the so-called "gravitational-arc tomography", that uses giant bright lensed arcs as background sources to map the CGM of *foreground* galaxies providing a tomographic view of the absorbing gas (????). The second one takes advantage of deep three-dimensional datacube observations to study the cold CGM of high-redshift ( $z > 2$ ) star-forming galaxies, and has reported the ubiquitous presence of Ly $\alpha$  haloes in these galaxies (????), whose line properties are correlated to their spatial location (?) and that can extend up to 4Mpc beyond the CGM (??). The third one uses the spectra of bright afterglows of long gamma-ray bursts (GRBs) to derive the kinematic properties of the CGM gas around their host galaxies and constrain the physical properties (??).

Alongside these diverse techniques to study the CGM, the large spectroscopic extragalactic surveys have allowed for the statistical extraction and analysis of the weak signals from different metal absorption using the stacking of hundreds of spectra (?). These large datasets have been helpful to overcome the limitations of finding galaxy-QSOs pairs at concordant redshifts (??), increasing statistics and facilitating vast parameter space exploration (???). At low-redshift ( $z_{\text{med}} \sim 0.5$ ) CGM analyses have been focused on the study of Ly $\alpha$  (?), C iv (?), O vi (?), Mg ii (???) absorption lines, and their dependence with stellar mass (?), inclination (?), and azimuthal angle (??). At higher redshifts, the observed metal absorption lines are mostly limited to Si ii, C ii, C iv, and Si iv, where the first two are called low-ionization state (LIS,  $T=10^{4-4.5}\text{K}$ ) lines, while the last two high-ionization state (HIS,  $T=10^{4.5-5.5}\text{K}$ ) lines (?). At high redshift ( $z>2$ ) several authors have reported the presence of high-velocity outflows. ? demonstrated that O vi successfully probe outflows in star-forming galaxies and reported velocity widths in the range  $200\text{--}400\text{km s}^{-1}$ . Next, ? analysed several ionization lines (e.g. Si ii, Fe ii, Al ii, Ni ii, Al iii, C iv) to probe the multiphase nature of the CGM and detected C iv blueshifted offsets concordant with  $76\text{km s}^{-1}$  velocity outflows. Their results show a direct link between C iv absorption and star formation rate. Later on, ? reported velocity outflows of  $\sim 150\text{km s}^{-1}$  as shown by several LIS and HIS absorptions in nine gravitationally lensed star-forming galaxies ( $z \simeq 2 - 3$ ), suggesting that galaxy outflows regulate the galaxy chemical evolution. Similar outflows detections inferred from different ionization absorption lines have been reported, and where stellar mass and star-formation rate have been invoked as their main drivers (????). However, as suggested by ? LIS and HIS absorption detections (from which velocity outflows can be inferred), could be affected by large-scale envi-

ronmental processes (??) or their available neutral gas content (???), and their correlation with stellar mass and star-formation rate, in fact, might be a consequence of a main-sequence offset, rather than simply correlated with their star-formation rate or stellar mass (??).

Numerical simulations consider that the CGM comes from gas accreted from the intergalactic medium (IGM), followed by stellar winds from the central galaxy and the gas ejected or stripped from satellites (??). Simulations reveal that the accretion efficiency depends on the galaxy stellar mass, decreasing from  $\sim 80$  per cent for  $M_{\star} \sim 10^6 M_{\odot}$  galaxies to  $\sim 60$  per cent for  $M_{\star} \sim 10^{10} M_{\odot}$  galaxies (???). Once accreted, this material can remain in the CGM for billions of years leading to a well mixed-halo gas before it interacts with the ejected large-scale stellar winds produced by starbursts (??). At  $z = 2$ , most metals are found to be located in the interstellar medium (ISM) or stars of the central galaxy and by  $z = 0.25$  most of it will end up in the CGM and IGM (e.g., ?????).

The way in which this pristine material is accreted into galaxies may depend on its location relative to the galaxy disk plane defined by the azimuthal angle ( $\phi$ ). Various observational studies highlight a correlation between the strength of the Mg ii LIS absorption line and the azimuthal angle (????). Although weak Mg ii detections along the minor axis have been reported (e.g., ?), it has been found that strong Mg ii absorptions are preferably detected along the major-axis of galaxies, suggesting the presence of inflowing material potentially feeding future star formation. On the other hand, C iv and O vi (HIS lines) absorptions seem stronger along the minor axis, probably evidencing strong stellar winds enriching the CGM (??). Recently, ? used cosmological hydrodynamical simulations to examine the physical properties of the gas located in the CGM of star-forming galaxies ( $z < 1$ ) as a function of angular orientation. They found that the CGM properties vary strongly with the impact parameter, stellar mass, and redshift. They reported a higher average CGM metallicity at large impact parameters ( $b > 100\text{kpc}$ ) along the minor versus major axes. Moreover, they tentatively found that the average metallicity of the CGM depends on the azimuthal angle, showing that the low metallicity gas is preferably inflowing along the galaxy major axis, while outflows are commonly located along the minor axis, concordant with previous observations (????). These results frame a picture where star-forming galaxies accrete co-planar gas within narrow stream-flows providing fresh fuel for the new generation of stars; later, this population will produce metal-enriched galactic-scale outflows along the minor axis (?). However, even though the presence of bipolar outflows collimated along the minor axis is expected to evolve with redshift (expected to be ubiquitous at  $z = 1$ ), it has been difficult to demonstrate its presence at  $z = 2$ , mostly as the result of the absence of gaseous galactic discs sculpting the outflows (?).

In order to better understand the mechanisms of galaxy growth in earlier phases of the history of the Universe, and to investigate a possible cosmic evolution of such mechanisms, similar studies at higher redshifts are needed. Observations along different lines of sight (l.o.s.) can probe different parts of the CGM, and the identification of low and high ionization metal absorption lines can give information on the possible multi-phase nature of the CGM. However, using QSO-galaxy pairs to study the CGM, is not straightforward, as the identification of the galaxies responsible for the metal absorptions detected on the spectra of background quasars, is not an easy task. Stacking analyses of *background* galaxy spectra that are located in the vicinity of *foreground* galaxies provide an alternative tool to overcome sen-

sensitivity limitations, exploiting large extra-galactic surveys containing a large number of individual spectra. In this work, we seek to characterize the presence of low- (LIS: O I+Si II, C II, Si II, Fe II), intermediate- (IIS: Al III) and high-ionization (HIS: Si IV, C IV) state metal absorption (see Table 2) in the CGM of a star-forming galaxy population at  $\langle z \rangle \sim 2.6$  using UV spectra obtained from the large VIMOS Ultra Deep Survey (VUDS; ?). We use thousands of galaxies with the most reliable redshift measurements and the highest S/N spectra (with reliability flags 3 and 4; see ??), a sample broadly representative of the bulk of the star-forming galaxy population at these redshifts (?). To detect the dim signal coming from low- and high ionization line absorptions produced in the CGM of these star-forming galaxies, we stack the spectra of close (in projection) *background* galaxies to establish the metal distribution in the CGM and explore their dependence on the physical and morphological properties of star-forming galaxies (e.g., impact parameter  $b$ , star formation rate, stellar mass, galaxy effective radius and azimuthal angle) at the peak epoch of cosmic star formation activity in the Universe.

The manuscript is organized as follows. Section 2 summarizes the VUDS survey properties relevant to our analyses. Section 3 presents our stacking analysis method for measuring the metal equivalent widths ( $W_0$ ), while Section 4 presents our  $W_0$  results for Ly $\alpha$ , and multiple LIS, IIS and HIS metal lines observed our star-forming galaxy sample across different physical and morphological properties. We discuss our results in Section 5, and finally we present our conclusions in Section 6. Throughout the text, we use  $\Lambda$ CDM cosmology with  $H_0 = 70 \text{ km s}^{-1} \text{ Mpc}^{-1}$ ,  $\Omega_M = 0.3$  and  $\Omega_\Lambda = 0.7$ , and distances are given in physical units (kpc).

## 2. The VUDS parent sample

VUDS has obtained spectra of 5590 galaxies in the redshift range  $1.5 < z < 4.5$ , the methods applied to process the data, and the derived parameters including the spectroscopic redshifts  $z_{\text{spec}}$  is given in ?. A description of the VUDS-DR1 first data release can be found in ?. The VUDS spectroscopic targets are selected based on their photometric redshifts and observed optical flux; the targets have  $z_{\text{phot}} + 1\sigma_z \geq 2.4$  and  $i_{AB} \leq 25$ . The wavelength range of each spectrum is between  $3600 < \lambda/\text{\AA} < 9350$ , accumulating 14 hrs of integration time in each of the LRBLUE and LRRED grisms of the VIMOS spectrograph on the ESO Very Large Telescope (?), with a spectral resolution  $R \sim 230 (\sim 7 \text{\AA})$  and reaching a S/N=5 on the continuum at  $8500 \text{\AA}$ . We note that the VUDS observations were taken using the VIMOS low-resolution multi-slit mode with a minimum slit length optimized to 6 arcsec, maximizing the number of observed slits per mask (see ?).

Standard data processing was performed using the VIPGI environment (?), followed by redshift measurements using the EZ package (?). The final UV rest-frame flux-limited sample is broadly representative of the bulk of the star-forming galaxy population at these redshifts ( $2 < z < 5$ ) (?). A critical aspect of VUDS is the large comoving volume covered, totalling of  $1 \text{ deg}^2$  in three fields: COSMOS (?), ECDFS (?), and VVDS02h (?).

For the purposes of this study, the instrumental setup translates into the ability to follow lines redder than Ly $\alpha$  ( $\geq 1215.6 \text{\AA}$ ) at redshifts higher than 1.5. We decided to restrict the VUDS sample to 2100 galaxies, selected in the redshift range  $1.5 < z < 4.5$  ( $z_{\text{flag}} = 3, 4$ , i.e. 95 – 100% probability of being correct). We note that the velocity accuracy of redshift measurements is expected to be in the range  $dz / (1 + z) = 0.0005\text{--}0.0007$ , or an

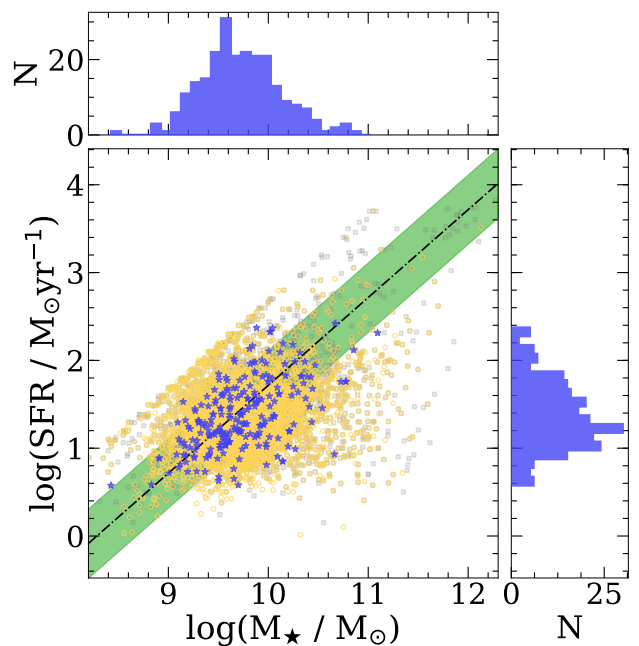


Fig. 1: SFR versus stellar mass for 5590 star-forming galaxies selected from the VUDS survey, at  $z > 1.5$  (gray open squares),  $2 < z < 3.5$  (yellow crosses) and the 238 star-forming galaxies (blue stars) considered in this work. The black dot-dashed line shows the main sequence of star-forming galaxies (SFG) for  $1.5 < z < 2.5$  including its  $\pm 0.3$  dex scatter represented by the green shaded region, as defined by ?. The top and right panels report the distributions in stellar mass and SFR, for the 238 star-forming galaxies evaluated in this work.

absolute velocity ( $\sigma_v^{-1}$ ) accuracy 150–200 km (???). The rich broadband imaging available for galaxies in VUDS is used for spectral energy distribution (SED) fitting (??) using the Galaxy Observed-Simulated SED Interactive Program (GOSSIP; ?) to derive various global galaxy properties (e.g., stellar mass, SFR, dust extinction  $E(B-V)$ , age, or metallicity).

GOSSIP is a tool that performs SED fitting by using a combination of spectro-photometric measurements from different bands to match a set of synthetic galaxy spectra based on emission from stellar populations. GOSSIP uses model spectra from galaxy population synthesis models (??) and uses the probability distribution function (PDF) of each galaxy parameter to determine the best SED fit. Figure 1 shows SFR versus stellar mass for 5590 star-forming galaxies at:  $z > 1.5$  selected from the VUDS survey (gray squares),  $2 < z < 3.5$  (yellow crosses) and the 238 star-forming galaxies (blue stars) that we finally selected and scrutinized in this work (see Section 3). These 238 galaxies have stellar masses and star formation rates of  $\log[M_\star/M_\odot] = 9.73 \pm 0.4$  and  $\log[\text{SFR}/(M_\odot \text{yr}^{-1})] = 1.38 \pm 0.39$ .

Exploiting the Hubble Space Telescope (HST)  $F814W$  images (?) that are available as part of the COSMOS Survey (?), morphological parameters have been estimated for 1242 star-forming galaxies ( $z_{\text{flag}} = 4, 3, 2, 9$ , i.e. 75% probability of being correct) with  $9.5 < \log[M_\star/M_\odot] < 11.5$ . In particular, ? run GALFIT (??), a standard parametric profile-fitting tool, estimating Sersic indices ( $n$ ), azimuthal angles, major to minor axis ratios ( $q$ ) and effective radii ( $r_{\text{eff}}$ ). Figure 2 shows the distribution of the 97 selected galaxy pairs (see Section 3) with available morphologi-

Table 1: VUDS *fg-bg* galaxy pair sample.

Sample	N
Galaxies $z > 1.5$ , $z_{\text{flag}}=3,4,2,9^a$	5590
Galaxies $z > 1.5$ , $z_{\text{flag}}=3,4^b$	2100
<i>fg-bg</i> galaxy pairs, $z_{\text{flag}}=3,4^c$	238
Galaxies fitted with GALFIT, $z_{\text{flag}}=3,4,2,9^d$	1242
<i>fg-bg</i> galaxy pairs, $z_{\text{flag}}=3,4 + \text{GALFIT}^e$	97

**Notes.** Number of objects of our *fg-bg* galaxy pair sample (see Sect. 2 for details).

<sup>(a)</sup> VUDS parent sample. <sup>(b)</sup> Star-forming galaxies at  $z > 1.5$ . <sup>(c)</sup> Star-forming galaxies with morphological parameters available. <sup>(d)</sup> Close *fg-bg* galaxy pairs. <sup>(e)</sup> Close *fg-bg* galaxy pairs with morphological parameters.

cal parameters. Table 1 shows the detailed number of subsets of galaxies.

### 3. Analysis

In this work, we seek to probe the CGM around galaxies at  $z \sim 2.6$ , near the epoch at which the cosmic star formation rate density of the Universe reaches its peak, by using the spectra of *background* (*bg*) galaxies as "spotlights" illuminating the CGM. At these redshifts, individual *bg* galaxies are not bright enough to individually detect low- and high-ionization state metal absorption lines. Thus, we stack spectra of *bg* galaxies to look for absorption lines produced by the CGM around *foreground* (*fg*) star-forming galaxies. To select a sample of close galaxy pairs (*fg-bg*) out of the VUDS survey, we have imposed similar criteria as those described by ?? : (i) galaxy spectra for the *fg* and *bg* galaxies must possess an accurately determined redshift (95 – 100% see ?? for details), (ii) a redshift separation  $0.1 < z_{\text{bg}} - z_{\text{fg}} \leq 1.0$  between *fg-bg* galaxy pairs to ensure that each spectrum contains a significant common spectral coverage after shifting to the rest-frame of the *fg* galaxy and avoid an overlap between the *fg* CGM and the *bg* galaxy absorptions., and iii) a maximum projected angular separation of  $23''$ .

Stacking the *fg* spectra provides the absorptions at the foreground galaxy's rest-frame. Figure 3 shows the redshift distributions of the *foreground* (red) and *background* (blue) galaxy pairs and the *fg-bg* pairs redshift difference ( $\Delta z = z_{\text{bg}} - z_{\text{fg}}$ ) distribution on the top-right corner. The spectroscopic sample includes 238 spectra within the redshift range  $1.5 < z \leq 4.43$  ( $\langle z \rangle = 2.6 \pm 0.41$ ) and is limited to a  $23''$  maximum projected angular separation distance amongst galaxy pairs, that correspond to  $187.2 \text{ kpc}$  at  $z=2.6$ . This sample is then split into four different bins according to their angular projected separation:  $\theta \leq 11''.8$ ,  $11''.8 < \theta \leq 16''.5$ ,  $16''.5 < \theta \leq 20''$ , and  $20'' < \theta \leq 23''$ , identified as samples S1, S2, S3, and S4 and were defined in such a way that each bin contains approximately the same number of galaxies (see Table 3) providing a comparable S/N for each composite spectra. These angular projected separation bins correspond to projected physical distances (hereafter impact parameters)  $b$ :  $b \leq 68.6 \text{ kpc}$ ,  $68.6 \text{ kpc} < b \leq 113.5 \text{ kpc}$ ,  $113.5 \text{ kpc} < b \leq 146.2 \text{ kpc}$ , and  $146.2 \text{ kpc} < b \leq 172.8 \text{ kpc}$  for samples S1, S2, S3, and S4. We note that the conversion from angular separation to physical impact parameter varies  $\pm 3\%$  over the full redshift range ( $1.5 < z < 4.5$ ) of the *foreground* galaxy sample, thus in the following impact parameter  $b$  and projected angular separation  $\theta$  will be interchangeably used. Table 3 contains a

summary of the statistical properties of the galaxy pair samples.

To generate our *fg* and *bg* composite spectra we co-added individual spectra as follows. For each pair of galaxies, the spectrum of the *fg* was:

1. shifted to its own rest-frame;
2. continuum-normalized using the full wavelength range<sup>1</sup>;
3. resampled<sup>2</sup> to a common wavelength resolution  $\Delta\lambda$ , defined by the maximum of the shifted wavelength resolution ( $\Delta\lambda_{\text{shf-}fg}$ ) distribution of the galaxy sample used to generate the composite spectra (e.g.  $\Delta\lambda \sim 2\text{\AA}$  for *fg* composite spectra as shown in Figure 4);
4. smoothed with a Gaussian kernel with width size  $\Delta\lambda$  defined before.

A similar approach was used to produce stacked spectra of the *bg* galaxies, each individual *bg* galaxy spectrum was:

1. shifted into the *fg* galaxy's rest-frame using the same systemic redshift applied to their corresponding *fg* galaxy spectrum;
2. continuum normalized using the full wavelength range<sup>1</sup>;
3. resampled to a common wavelength resolution  $\Delta\lambda$ , defined by the maximum of the shifted wavelength resolution ( $\Delta\lambda_{\text{shf-}bg}$ ) distribution of the galaxy sample used to generate the composite spectra;
4. smoothed with  $\Delta\lambda$  Gaussian kernel as defined before;
5. masked the strong interstellar absorption features (see Fig 4 and Table 2) located at the redshift of each *bg* rest-frame that can potentially contaminate the composite signal at the *fg* rest-frame.

Finally, the *foreground* and *background* spectra were co-added independently to produce composite stacked spectra; in all cases, for each spectral bin, we calculated both the average and the median value, eventually producing both an average and median co-added spectrum.

### 4. Results

Rest-frame UV spectra of star-forming galaxies at redshift  $z \sim 3$  are commonly dominated by the emission of O and B stars; the CGM and/or IGM media imprint absorption features on top of this UV continuum (????). Composite spectra can provide different l.o.s. of the average absorption strength produced by the gas located in these media (??). Figure 4 shows the median and average composite spectra by stacking the 238 *foreground* galaxies. The lower panel shows a histogram of the fraction of galaxies contributing to each spectral bin of the co-added spectrum. In our analysis, the separation zero ( $b = 0$ ) l.o.s. defines the interstellar medium properties of the *foreground* galaxies, while larger separations ( $b > 0$ ) l.o.s. define the properties of the CGM around the *foreground* galaxies at different separations.

While the l.o.s. that we use to study the CGM cross through the whole CGM at a given separation, the information about the ISM comes only from the absorptions produced by the gas located in the half galaxy that is the closest to the observer. For this reason, to compare the strength of the absorptions at separation 0 (e.g. the ISM) and at separation  $> 0$  (e.g. the CGM),

<sup>1</sup> Full observed wavelength coverage:  $3650 < \lambda < 9350 [\text{\AA}]$  which at  $z \sim 2.6$  translates into a rest-frame wavelength coverage:  $1013 < \lambda < 2597 [\text{\AA}]$

<sup>2</sup> We have made use of PYSYNPHOT (?) to resample our spectra.

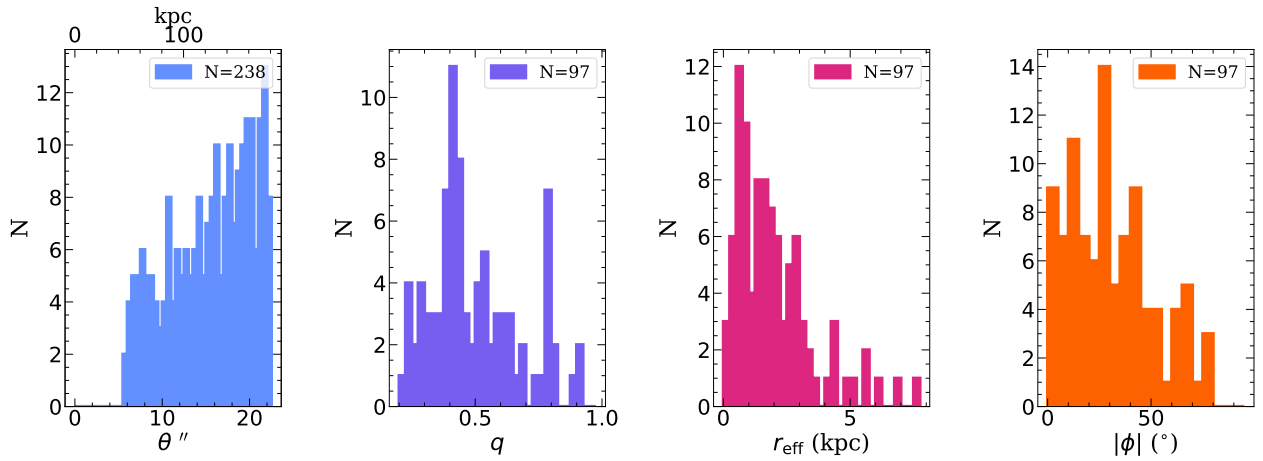


Fig. 2: Projected angular separation ( $\theta$ ) amongst galaxy *foreground-background* galaxy pairs, axial ratio ( $q$ ), effective radius ( $r_{\text{eff}}$ ) and azimuthal angle ( $\phi$ ) distributions of the star-forming (*foreground*) galaxies used in our analyses. Morphological parameters were obtained from the parametric measures of  $\mathcal{P}$ , see section 2 for details.

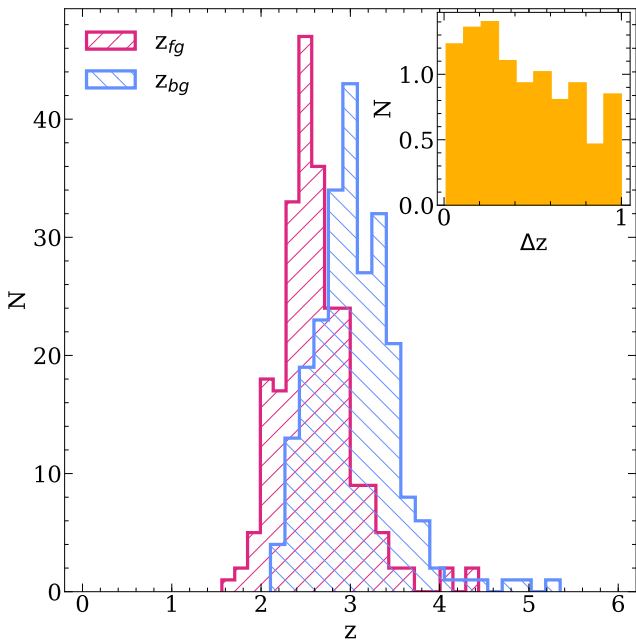


Fig. 3: Redshift distribution of the star-forming galaxy pairs (*foreground* and *background*) selected in this work. The  $\Delta z = z_{bg} - z_{fg}$  distribution is also included in the top-right corner.

the former need to be corrected for this incompleteness. Following  $\mathcal{P}$ , we apply the following factors: 1.45 for low-ionization species (Si II, C II), 1.70 for Si IV and  $\sim 2$  for C IV. The different I.O.S. probed by the *background* galaxy's light passing through the *foreground* CGM help us to trace neutral and ionized gas in HII star-forming regions and the large-scale stellar winds produced by star-formation activity ( $\mathcal{P}$ ). The main spectral features identified in our *fg* composite spectra (Figure 4) in the 1100–2000 Å range are summarized in Table 2 and include: H I (Ly $\alpha$ ) emission/absorption (blue), low-ionization state metal absorption lines (cyan), intermediate-ionization state metal absorption lines (peach), high-ionization state metal absorption lines (magenta), interstellar fine-structure emission line (green), absorption stellar photospheric lines (gold), emission nebular

Table 2: Main spectral features observed in our VUDS stacked spectra in the 1100–2000 Å rest-frame range.

Spectral line	$\lambda$ [Å]	Type
C III	1176	Photospheric
Si II	1192	LIS absorption
Si III	1206	IIS absorption
Ly $\alpha$	1215.7	H I
N V	1238/1242	Photospheric
Si II	1260	LIS absorption
Si II*	1264.0	Interstellar
O I+Si II	1303.2	LIS absorption
Si II*	1309.0	Interstellar
C II	1334.5	LIS absorption
O IV	1343.0	Photospheric
Si IV	1393.8/1402.8	HIS absorption
Si III	1417	Photospheric
S V	1501.8	Photospheric
Si II	1526.7	LIS absorption
C IV	1548.2/1550.8	HIS absorption
Fe II	1608,	LIS absorption
Fe II	1610,	LIS absorption
He II	1640	Stellar wind
O III]	1660/1666	Nebular
Al II	1670.7	LIS absorption
Ni II	1709.6	LIS absorption
N IV	1718.5	Stellar wind
Ni II	1741.5/1751.9	LIS absorption
Si II	1808	LIS absorption
Al III	1854.7/1862.7	IIS absorption
Si III]	1889	Nebular
C III]	1908.7	Nebular

lines (lime), and emission/absorption lines associated with stellar winds (indigo)( $\mathcal{P}$ ; OTELO<sup>3</sup>).

In the 900–1900 Å range, we have explored the following absorption lines: Ly $\alpha$  ( $\lambda$  1215.7 Å), O I+Si II ( $\lambda$  1303.2 Å), C II ( $\lambda$

<sup>3</sup> OSIRIS Tunable Emission Line Object survey <http://research.iac.es/proyecto/otelo/pages/data-tools/spectral-line-summary.php>



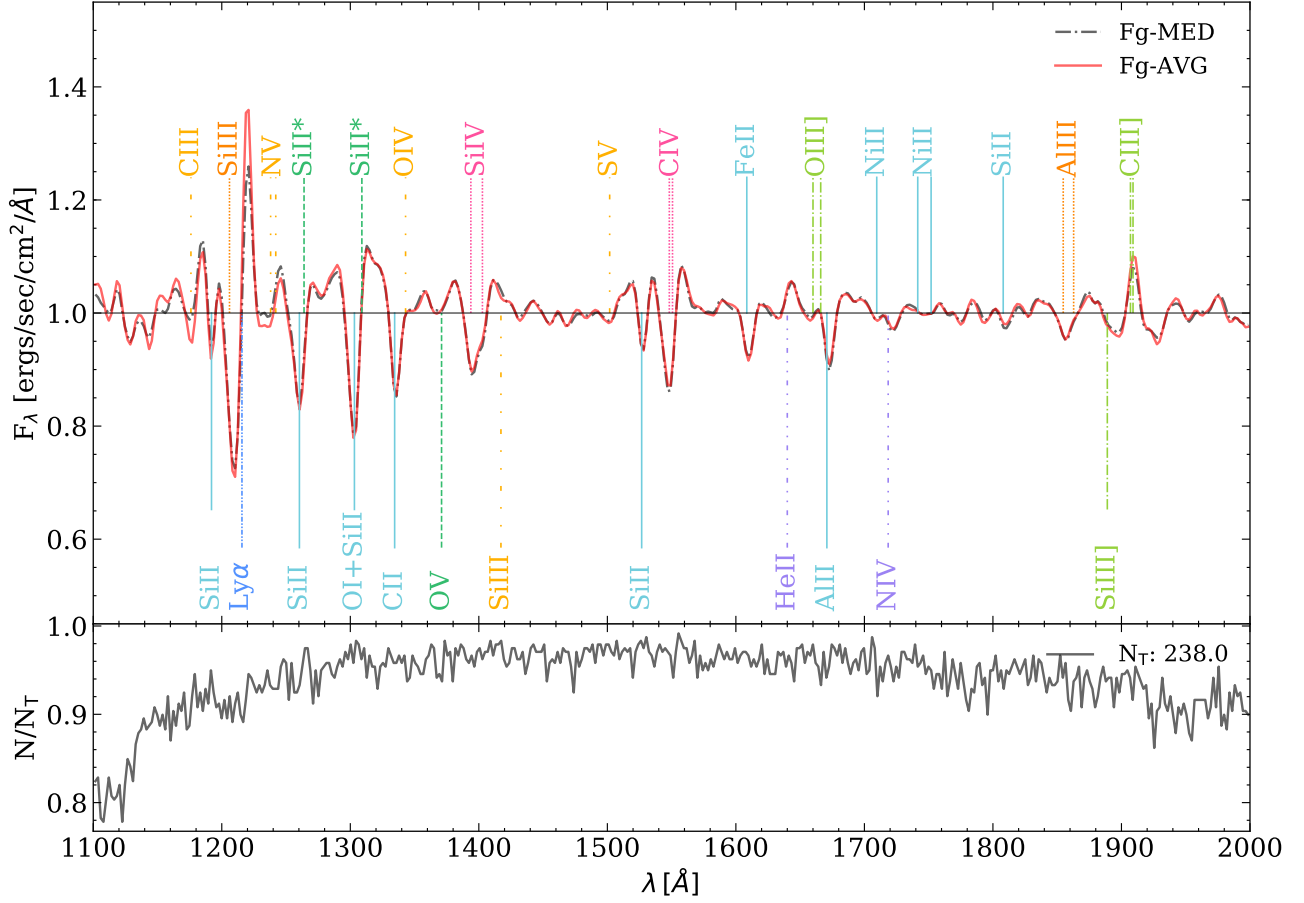


Fig. 4: Top: Median (black) and average (red) composite spectra shifted to rest-frame of 238 *foreground* galaxies with projected angular separations  $< 23''$  ( $b < 187.2$  kpc at  $z=2.6$ ). Bottom: The fraction of contributing individual spectra to the composite spectra per unit wavelength. Several spectral lines of interest are marked: H I (Ly $\alpha$ ) emission/absorption (blue), low-ionization state metal absorption lines (cyan), intermediate-ionization state metal absorption lines (peach), high-ionization state metal absorption lines (magenta), interstellar fine-structure emission line (green), absorption stellar photospheric lines (gold), emission nebular lines (lime), and emission/absorption lines associated with stellar winds (indigo).

Table 3: *Foreground-background (fg-bg)* galaxy pair statistics according to their projected angular separation ( $\theta$ ).

ID	N	$\theta$	$\langle\theta\rangle$	$b$ (kpc)	$\langle b \rangle$ (kpc)	$z_{fg}$	$\langle z_{fg} \rangle$	$z_{bg}$	$\langle z_{bg} \rangle$
c1	c2	c3	c4	c5	c6	c7	c8	c9	c10
ALL	238	$< 23''$	$15''.7 \pm 4''.9$	13.8 - 187.2	$125.0 \pm 39.5$	1.5-4.4	2.60	2.1-5.3	3.04
S1	59	$< 11''.8$	$8''.7 \pm 2''.0$	13.8 - 97.8	$68.6 \pm 16.3$	1.5-4.3	2.55	2.1-4.9	2.98
S2	62	$11''.8-16''.5$	$14''.4 \pm 1''.4$	92.6 - 135.9	$113.5 \pm 12.8$	1.7-4.3	2.62	2.1-4.9	3.08
S3	60	$16''.5-20''$	$18''.4 \pm 0''.9$	127.1 - 164.6	$146.2 \pm 8.8$	1.9-3.6	2.66	2.3-4.5	3.11
S4	57	$20''-23''$	$21''.5 \pm 0''.8$	146.7 - 187.2	$172.8 \pm 8.4$	1.8-4.4	2.59	2.1-5.3	3.02

**Notes.** Column 1: Sample ID; Column 2: number of galaxies per sample; Column 3: range of angular separation of the *fg-bg* pairs; Column 4: mean angular separation of the *fg-bg* pairs within the  $\theta$  range; Column 5: range of the impact parameter in kpc assuming  $z_{med}$  within the projected separation bin for conversion; Column 6: mean impact parameter within the  $\theta$  range in kpc; Column 7 and 8: redshift ranges and mean redshift of the *foreground* galaxies sample within their corresponding  $\theta$  range, and Columns 9 and 10: redshift ranges and mean redshift of the *background* galaxies sample within their corresponding  $\theta$  range.

1334.5 Å), Si IV ( $\lambda\lambda$  1393-1402 Å), Si II ( $\lambda$  1526.7 Å), C IV ( $\lambda\lambda$  1548.2-1550.8 Å), Fe II ( $\lambda$  1608.5 Å), Al II ( $\lambda$  1670.8 Å) and Al III ( $\lambda$  1862.8 Å). First we present their equivalent widths as a function of the angular separation between galaxy pairs ( $\theta$ ) (see Sect. 4.1). We then examine the correlations between the strength of Ly $\alpha$ , LIS (C II, Si II) and HIS (C IV, Si IV) lines as a function of

different galaxy properties, including stellar mass, star formation rate (see Sect. 4.2), effective radius ( $r_{eff}$ ) and the azimuthal angle ( $\phi$ ) (see Sect. 4.3). We also explore the C II/C IV line ratio (see Sect. 4.4) as a function of the projected angular separation, stellar mass, and star formation rate.

#### 4.1. Radial dependence

Here we present absorption lines produced by gas located in the CGM of star-forming galaxies at  $z \sim 2.6$ . Figure 5 shows the average absorption spectra obtained after stacking the *background* galaxy spectra at the redshift of the *foreground* galaxy as a function of their projected angular separation:  $< 11''$ ,  $11''$ – $16''$ ,  $16''$ – $20''$  and  $20''$ – $23''$ . We note that as a consequence of VUDS design and selection criteria, the number of galaxies with small projected angular separations ( $< 6''$ ) is scarce. The strengths of the line absorptions were measured by fitting a single Gaussian profile to the stacked spectra. Equivalent widths ( $W_0$ ) of each line profile are obtained by integrating the Gaussian fit of each stacked spectrum around the central wavelength of the Gaussian fit to the line using an integration window within the  $\pm 5\sigma$  range.

All equivalent width measurements are given in the rest-frame and we use positive (negative) equivalent widths to indicate absorption (emission). The errors on the equivalent width measurements are determined using a bootstrap approach. For each set of galaxy *background* spectra, a thousand co-added spectra are generated from random selections, with replacements, from that same sample, preserving the number of evaluated sources. For each of these co-adds, the line absorption equivalent widths are estimated. The 16th/84th percentiles of the distribution of equivalent widths are taken as error intervals for the original measurement. We note that owing to the nature of star-forming galaxies, that show a diversity of spectral features (e.g., ISM absorption lines, photospheric stellar lines/nebular lines, and Ly $\alpha$  emission), the absorption lines in our composite spectra show both an emission and absorption component. The emission components can be produced by the same transition responsible for producing the absorption line (e.g. Ly $\alpha$ ), produced by nearby fine-structure transitions or in some cases they can be completely absent.

Figure 6 shows the radial profiles of the absorption rest-frame equivalent width obtained from the average (red) and median (blue) stacked absorption spectra presented in Figure 5. Median composite spectra are expected to be free of artefacts and contamination such as sky residuals, unexpected absorption/emission features in the *background* galaxy spectra. On the other hand, the average composite spectra could be affected by strong absorption lines coming from individual I.o.s. Median and average composite spectra are in general concordant, tracing similar trends. We also tested other combination techniques, including straight average, average-sigma-clipping and average-continuum-weighted, that produce very similar composite spectra. Table 4 contains a summary of the measured equivalent widths as a function of the projected angular separation, including the significance (in terms of S/N) of the detections. Noise estimations were computed with the DER\_SNR<sup>4</sup> algorithm (?) on continuum band-pass adjacent to each central absorption line. We limit our analyses to detections with  $S/N \geq 3$ , however, upper limits with  $S/N < 3$  are also included and highlighted using solid black symbols and arrows in Figure 6, as these detections are useful to outline the possible correlations/trends of the profiles. We note that some precautions should be taken when interpreting the absorption strengths of these spectral features as they could not reflect the true conditions of the cold and hot gas CGM components. For instance, the balances amongst singly ionized species of some elements (e.g. Al, Cl) can be altered by dielectronic recombination (???) or ion-molecule reactions(charge exchange reactions of ionized species with neutral hydrogen and

helium ?). In fact, while the abundances relative to neutral hydrogen of some elements (e.g. O, N, P, Cl, Si, Cr, Mn, Fe, Ni) can be affected by factors of 2-10, Al is depleted by a factor of  $\sim 100$  (?), making Al II a biased tracer of the neutral gas phase. In addition, Fe II is contaminated by Fe IV ( $\lambda$  1610 Å) and Fe II ( $\lambda$  1611.5 Å) lines (???), making it difficult to determine accurately its absorption strength. Subsequently, double ionized species (e.g. Si III, Al III) are intermediate-ionization state (IIS) tracers of moderately photoionized warm gas sensitive to both diffuse ionized gas (traced by H II) as well as denser, partly neutral gas. Depending on the species they can be correlated with cold (e.g. Si III ?) or hot gas components (e.g. Al III ?) and they can be used to infer the relative mix of neutral and ionized material (?).

We note, that the composite spectra considering *foreground* (down-the-barrel) galaxies from our *fg* – *bg* galaxy pairs split by separation, do not show any significant dependency of the  $W_0$  of absorption lines with impact parameter  $b$ , that show an average variance of  $\leq 15\%$  amongst the absorption lines included in 6. This is in agreement with the  $< 10\%$  variance that ? reported for their brightest absorption lines. Considering the *background* galaxies from our *fg* – *bg* galaxy pairs split by separation, our radial profiles show a general negative gradient as reported by previous works. As the impact parameter increases, the strength of the detected absorption feature decreases. This is the case for all the spectral lines considered in our analysis. Recently, ? compiled measurements of low-ionization state absorption lines(O I, C II, N II, Si II), and high-ionization state absorption lines(C III, N III, Si III, C IV, Si IV, N V, and O VI) in the CGM of low-redshift( $z \leq 0.3$ ) galaxies with  $9 \leq \log[M_\star/M_\odot] \leq 11$ , using quasars as background spotlights. Measurements at low redshift (?????) and high-redshift ( $z \sim 2.3$ ) galaxies (?) are also overplotted in Figure 6.

Although at low redshift these lines can be detected at distances up to 300 kpc, at high redshift using galaxy-galaxy pairs, ? reported detections that are limited to 100 kpc; including 42 additional bright quasars-galaxy pairs that provide access to the low-density gas in the CGM, they extended their Ly $\alpha$  detections up to 280 kpc. More recently, using galaxy images at  $\langle z \rangle \sim 2.4$ , ? measured the Ly $\alpha$  excess relative to the background intergalactic medium, probing the CGM gas up to impact parameters of 2000 kpc. Here, for star-forming galaxies at a mean redshift  $\langle z \rangle = 2.6$ , we report detections at distances up to 146 kpc and 172 kpc for H II and LIS/Ly $\alpha$ . These results include Al III, which is detected for the first time in the CGM of high-redshift star-forming galaxies up to distances of  $\sim 150$  kpc. Low-ionization state lines (C II, Si II, Al II) show less steep radial profiles compared with high ionization lines. The LIS radial profile shows an abrupt decay at smaller radii. From separation zero to  $\langle b \rangle \sim 68$  kpc, the strengths of C II, Si II, and Al II are reduced by a factor of 1.7, 2.5, and 3.2, while Si IV and C IV are reduced by a factor of 6.8 and 4.5.

? reported that at a separation of  $\langle b \rangle = 103$  kpc, lines can be hardly detected in their stacked spectra, low-ionization state metal absorption lines cannot be detected and C IV is detected with marginal significance. Here we are able to detect LIS (C II and Si II) and H II (Si IV, C IV) both with  $S/N \geq 3$  up to  $\langle b \rangle = 172$  kpc and 146 kpc separations. We note that beyond this separation ( $\theta > 23''=172$  kpc) we are unable to detect any significant signal from the *background* composite spectra. This might be caused by differences in the S/N and resolution of the individual spectra used in the two analyses. The spectral line features considered here are more difficult to detect in

<sup>4</sup> [http://www.stecf.org/software/ASTROsoft/DER\\_SNR/](http://www.stecf.org/software/ASTROsoft/DER_SNR/)

Fig. 5: Median absorption lines (thin lines) detected from our 238 *foreground-background* galaxy pairs, including all *foreground* galaxies (red) and *background* galaxies split by their projected angular separations:  $<11''.8$  (blue),  $11''.8$ - $16''.5$  (green),  $16''.5$ - $20''$  (cyan), and  $20''$ - $23''$  (magenta); bold lines indicate the Gaussian profile fit to measure the strength of the line absorptions (see Sect. 4.1).

Fig. 6: Rest equivalent width ( $W_0$ ) as a function of the impact parameter ( $b$ ) obtained from the line profiles in Fig 5, corresponding to the *foreground* composite spectra (0 kpc) and the *background* composite spectra at  $\langle b \rangle$  68.6 kpc ( $8''.7$ ), 113.5 kpc ( $14''.4$ ), 146.2 kpc ( $18''.4$ ) and 172.8 kpc ( $21''.5$ ). Average and median  $W_0$  are shown in solid-red and open-blue symbols, solid black symbols correspond to upper limits with SNR  $<3$ . Reported values from the literature including low-redshift values (open-gray symbols):  $\circ$  (stars),  $\square$  (pentagons),  $\times$  (crosses),  $\diamond$  (diamonds),  $+$  (pluses), and high-redshift values  $\blacktriangle$  (black triangles). Error bars correspond to  $1\sigma$  confidence intervals for average (red filled circles) or median (blue unfilled circles) values based on a bootstrap analysis. Additionally, the results from the Kendall-Tau correlation test: the correlation coefficients  $r_\tau$  and their corresponding  $p$ -value (probability of no correlation) are also included.

our low-resolution spectra compared to a high-resolution spectra at the same S/N level. Higher-resolution spectra could allow to resolve spectral lines that are blended (e.g. O I-Si II:  $\lambda\lambda$  1303-1307 Å, Si IV:  $\lambda\lambda$  1393-1402 Å), or that are affected by close photospheric/interstellar/nebular spectral lines (e.g. Fe II-Fe IV:  $\lambda\lambda$  1608-1610, Si II-Si II\*:  $\lambda\lambda$  1260-1264), disentangling the spectral features and thus provide a more accurate  $W_0$  measurements. Another possibility to explain these discrepancies, is that they might be the result of differences in the SNR of both parent dataset samples. We know that both parent samples adopted opposite observational strategies. On one hand,  $\circ$  deliberately kept short the total exposure times on their observations to maximize the number of galaxies for which redshifts could be measured. This led to a dataset with spectral quality (S/N) that varies considerably amongst their spectra ( $\circ$ ), and that could be affecting their redshift determinations. On the other, VUDS provide a homogeneous dataset with integration times of  $\approx 14$ h per target, allowing to reach a S/N on the continuum at 8500 Å of S/N=5 ( $\circ$ ). Moreover, in this work, we have considered galaxies with reliability flags ( $z_f = 3, 4$ ) with 95-100% probability of being correct. However, it is not clear if similar constraints on their redshift determinations were adopted by  $\circ$  to define their galaxy-galaxy pair sample. This is crucial, as composite spectra can be affected by spectral offsets in the individual spectra. LIS and HIS spectral absorptions could be washed out or artificially boosted by considering individual spectra with low SNR and low-reliability redshift determinations to generate composite spectra. In fact, the spectra considered to generate our stacked spectra may show an average SNR larger than the average SNR of the spectra considered by  $\circ$ . If similar separations ( $\langle b \rangle$ ) are considered, Steidel's P3 sample at  $\langle b \rangle = 103$  kpc ( $\langle \theta \rangle = 12''.5$ ) and this work S2 sample  $b = 113.5$  kpc ( $\langle \theta \rangle = 14''.4$ ), Steidel's P3 sample considers  $\sim 5$  times the number of objects (N=306) considered in our S2 sample (N=62). This would imply that our spectra have an average higher individual SNR compared to the average SNR of the dataset used by  $\circ$ , allowing us to detect similar/weaker spectral absorptions at larger separations.

To assess the correlation between  $W_0$  and  $b$ , we implemented a Kendall-Tau correlation test. The correlation coefficients  $r_\tau$  and their corresponding  $p$ -value (the probability of no correlation) are provided in the same figure. In all cases we find a robust anticorrelation of the strength of the absorption line as a function of the impact parameter: in particular, Ly $\alpha$ , C II, C IV, and Fe II all show a strong correlation ( $p < 0.05$ ), while we find that O I, Si IV, Si II, Al II, and Al III present a flatter radial profile with that results in a lower significance of the anti-correlation ( $p \sim 0.1$ ). To assess the scale of the relationship between  $W_0$  and  $b$ , we compute the

slopes of the radial profiles shown in Fig 6. We find that Ly $\alpha$  show a slope of  $-1.20 \pm 0.01$ , LIS: O I+Si II, C II, Si II, Fe II, and Al II absorption lines show slopes  $-1.34 \pm 0.01$ ,  $-1.31 \pm 0.01$ ,  $-1.53 \pm 0.02$ ,  $-1.50 \pm 0.07$ , and  $-1.44 \pm 0.05$ , Al III show a slope of  $-1.38 \pm 0.06$  and HIS: Si IV and C IV absorption lines show,  $-1.10 \pm 0.04$  and  $-1.24 \pm 0.01$ . If we focus on low and high ionization lines of the same species, and considered Si II-Si IV and C II-C IV absorption line pairs, we find that the slopes of these absorption lines are different at  $\geq 5\sigma$  level. Compared with  $\circ$  radial profiles, our results show slopes that are different at a  $5\sigma$  level for Si II and  $3\sigma$  level for C II and Al II absorption lines. These differences suggest that within the CGM, cold and dense gas is more spatially extended in galaxies at  $z \sim 2.6$  compared with galaxies at  $z \sim 2.3$  and lower redshifts, as probed by Si II C II, in agreement with the expected higher covering factors of neutral gas at higher redshifts ( $\circ$ ). Compared with low-redshift CGM studies (see Figure 6), our Ly $\alpha$ , LIS and HIS rest-frame equivalent width radial profiles are at the upper envelope of the equivalent width measurements at lower redshifts, suggesting a potential redshift evolution for the CGM gas content that produces these absorptions.

#### 4.2. Star formation and stellar mass Dependence

To explore the dependence of low- and high-ionization state absorptions with physical and morphological properties (i.e. star formation rate, stellar mass, galaxy effective radius and azimuthal angle) produced in the CGM of our high-redshift star-forming galaxy sample, we considered galaxy pairs at all projected distances ( $b < 23''$ ) split by the corresponding galaxy property. A summary of the statistical properties of the galaxy pair subsamples divided by these properties can be found in the Appendix A. We note that Fe II, Al III, and Al II lines were excluded from our following analyses (see sec 4.1) Figure 7 (upper panels) shows the equivalent width of the absorption features as a function of stellar mass and SFR for LIS (C II, Si II), HIS (Si IV, C IV) and Ly $\alpha$ . We find that galaxies with high stellar masses ( $\log[M_\star/M_\odot] > 10.30$ ) and high star formation rates ( $\log[\text{SFR}/(M_\odot \text{yr}^{-1})] > 1.93$ ) show C IV (HIS) metal absorption with larger equivalent widths. On the other hand, galaxies with low stellar masses ( $\log[M_\star/M_\odot] < 9.26$ ) and low SFRs ( $\log[\text{SFR}/(M_\odot \text{yr}^{-1})] < 0.9$ ) show C II (LIS) metal absorptions with stronger equivalent widths. Nevertheless, Si II and Si IV do not show a similar trend. This might be caused by the fact that we do not have Si II and Si IV detections with S/N>3 in all of our SFR and stellar mass bins.



Table 4: Median absorption line strengths measured ( $W_0$  Å) in stacked spectra as a function of the average impact parameter ( $\langle b \rangle$ ).

$\langle b \rangle$ (kpc)	$W_0$ [Å]	S/N	$W_0$ [Å]	S/N	$W_0$ [Å]	S/N	$W_0$ [Å]	S/N	$W_0$ [Å]	S/N
c1	c2	c3	c4	c5	c6	c7	c8	c9	c10	c11
Ly $\alpha$ 1215.7			O I-Si III 1303.2		C II 1334.5		Si IV 1393.8		Si IV 1402.8	
0.0	$3.54 \pm 0.02$	58	$2.61 \pm 0.15$	17	$2.31 \pm 0.08$	20	$1.91 \pm 0.01$	18	$1.40 \pm 0.05$	67
68.6	$1.71 \pm 0.13$	14	$0.97 \pm 0.10$	9	$1.37 \pm 0.02$	4	$0.28 \pm 0.06$	4	$0.32 \pm 0.06$	15
113.5	$0.75 \pm 0.05$	9	$0.59 \pm 0.07$	8	$0.54 \pm 0.01$	3	$0.09 \pm 0.04$	2	<0.10	<2
146.2	$1.08 \pm 0.13$	13	<0.26	<2	$0.30 \pm 0.09$	2	$0.13 \pm 0.19$	3	$0.27 \pm 0.31$	5
172.8	$0.46 \pm 0.14$	5	<0.39	<2	$0.38 \pm 0.10$	3	<0.09	<2	<0.06	<2
Si II 1526.7			C IV 1548.2		Fe II 1608.5		Al II 1670.8		Al III 1862.8	
0.0	$0.94 \pm 0.02$	18	$2.87 \pm 0.11$	20	$0.99 \pm 0.01$	6	$1.13 \pm 0.03$	10	$1.25 \pm 0.01$	8
68.6	$0.35 \pm 0.03$	3	$0.70 \pm 0.04$	13	$0.18 \pm 0.03$	3	$0.35 \pm 0.03$	4	$0.31 \pm 0.11$	7
113.5	$0.24 \pm 0.09$	2	$0.27 \pm 0.04$	2	<0.03	<2	$0.18 \pm 0.03$	3	<0.06	<2
146.2	$0.36 \pm 0.05$	4	$0.24 \pm 0.02$	3	—	—	—	—	$0.40 \pm 0.02$	3
172.8	$0.39 \pm 0.04$	4	<0.05	<2	—	—	—	—	<0.34	<2

**Notes.** *Foreground-background (fg-bg)* galaxy pairs split by their average impact parameters ( $\langle b \rangle$ ): 68.6 kpc (N=60), 113.5 kpc (N=62), 146.2 kpc (N=60), and 172.8 kpc (N=57). The errors on the equivalent width ( $W_0$ ) measurements correspond to  $1\sigma$  confidence intervals based on a Bootstrap analysis (see Sect. 4.1).

To quantify the robustness of the trends highlighted in Figure 7, we ran a Kendall-Tau rank test for the absorption lines that are detected in at least 3 bins. We find that SFR and stellar mass are anti-correlated with C II, but they correlate positively with C IV. This would imply that C II is located mostly in galaxies with low stellar mass ( $\log[M_\star/M_\odot] < 9.26$ ) and low SFR ( $\log[\text{SFR}/(M_\odot \text{yr}^{-1})] < 0.9$ ) while C IV is detected in galaxies with high stellar mass ( $\log[M_\star/M_\odot] > 10.2$ ) and high SFR ( $\log[\text{SFR}/(M_\odot \text{yr}^{-1})] > 1.5$ ). In fact, the slopes of the  $W_0$  relationships with stellar mass and SFR for C II and C IV are  $0.79 \pm 0.13$ ,  $0.61 \pm 0.05$  and  $0.73 \pm 0.08$ ,  $0.55 \pm 0.04$ , that are significantly different at  $\geq 5\sigma$  level. We do not find any robust correlation between SFR and stellar mass with Si II, Si IV, Fe II, Al II, Al III or Ly $\alpha$ , yielding a probability of no correlation above 60% in all cases. We also explored the combined effect of impact parameter with stellar mass and SFR; however, no clear conclusion was reached due to low-number statistics resulting in composite spectra with low S/N line detection.

#### 4.3. Morphological Dependence

The strength of the observed metal absorption signatures in the CGM can be explored as a function of the azimuthal angle  $\phi$  between the l.o.s. and the projected major/minor axis of the *foreground* galaxy. Here we define the azimuthal angle ( $\phi$ ) as the projected angle between the *background* galaxy l.o.s. and the projected minor axis of the *foreground* galaxy. Small azimuthal angles ( $\phi \sim 0^\circ$ ) refer to l.o.s. passing along the projected minor axis of the *foreground* galaxy, while large azimuthal angles ( $\phi = 90^\circ$ ) refer to l.o.s. passing along the projected major axis of the *foreground* galaxy. The effective radius ( $r_{\text{eff},\text{circ}} = r_{\text{eff}} \sqrt{q}$ <sup>5</sup>) was obtained by fitting a single Sérsic profile with no constraints in the parameters and then was circularized using the galaxy ellipticity (?). Alongside the effective radius, GALFIT provides other structural parameters: Sérsic index ( $n$ ), the axis ratio of the ellipse ( $b/a$ ) and the position angle,  $\theta_{\text{PA}}$ . Out of the 238 galaxies evaluated in this paper, only 97 are in the COSMOS field, covered by HST imaging, and therefore have morphological pa-

rameters. To inspect the dependency of the LIS-HIS absorption strengths with the azimuthal angle ( $\phi$ ), we split our sample into three  $\phi$  bins:  $[0-30]^\circ$ ,  $[30-60]^\circ$  and  $[60-90]^\circ$ . Figure 7 (lower panels) reports the equivalent width of different spectral features in bins of  $r_{\text{eff}}$  and  $\phi$ .

To check and assess the robustness of possible correlations between the morphological parameters and the equivalent widths measured in the composite spectra for LIS, HIS, and Ly $\alpha$ , we ran a Kendall-Tau rank test between  $W_0$  and  $\phi/r_{\text{eff}}$ . For lines detected in only two bins the correlation can not be assessed, therefore we estimated the significance of the difference between their absorption strength ( $W_0$ ). To do so, we applied a Student's t-test to determine the probability that the  $W_0$  variations between the low- and high  $r_{\text{eff}}/\phi$  populations are not statistically significant. According to the Student's statistics ( $t$ ) a large  $p$ -value indicates that a large probability of the null hypothesis to be correct (the two samples are not statistically significant); a small  $p$ -value suggests that the difference is significant. Both, Kendall-Tau and Student's t-test results are quoted in Figure 7 in the corresponding panels.

Regarding the effective radius ( $r_{\text{eff}}$ ) of the galaxy, the Kendall-Tau test shows a mild anti-correlation with C II ( $p < 0.117$ ), while it does not show any significant correlation with Si II and Si IV ( $p > 0.602$ ). We find a significant difference ( $p < 0.01$ ) in the  $W_0$  variations between small and large  $r_{\text{eff}}$  as shown by the Student's t-test. However, no correlation is found for Ly $\alpha$ . This suggests that C IV gas is usually located in the CGM of larger galaxies while C II gas is located in the CGM of smaller galaxies. Concerning the azimuthal angle, we do not find any significant correlation with  $\phi$  in any of the spectral lines inspected, in agreement with what has been reported by (?) who inspected the azimuthal dependence of Ly $\alpha$  emission of 59 star-forming galaxies ( $z_{\text{med}} \sim 2.3$ ). This is opposed to the low-redshift scenario, where galaxies show high-velocity biconical outflows oriented along the minor-axis and accreting material along the major-axis. This result could be linked to the metal distribution along the disk of star-forming galaxies as metal absorption systems are often compact and poorly mixed, where cool low-ionization metal absorbers have typical sizes of  $\sim 1$  kpc (?),

<sup>5</sup>  $q$  is the axis ratio ( $b/a$ ) of the elliptical isophotes that best fit the galaxy.

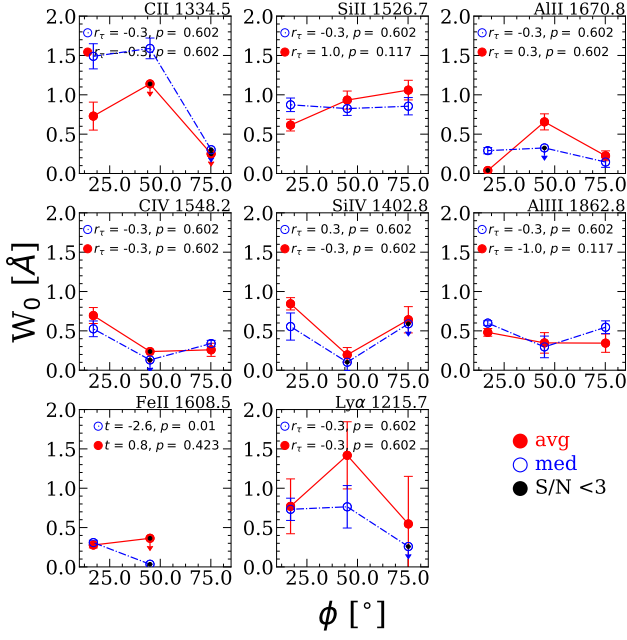


Fig. 7: Rest equivalent width ( $W_0$ ) of the absorption lines as a function of the *foreground* galaxy’s stellar mass ( $\log[M_\star/M_\odot]$ ), SFR ( $\log[M_\odot \text{yr}^{-1}]$ ), effective radius ( $r_{\text{eff}}$ ) and azimuthal angle ( $\phi$ ). The  $W_0$  measurements come from composite spectra considering galaxy pairs at all projected distances ( $b < 23''$ ) and split by the corresponding galaxy property. Stellar mass and SFR  $W_0$  were obtained from composite spectra considering 238 *bg* galaxies, while  $r_{\text{eff}}$  and  $\phi$  come from composite spectra considering 97 *bg* galaxies (see Sect. 2 and Table 1). Average and median  $W_0$  are shown in solid-red and open-blue symbols, solid black symbols correspond to upper limits with SNR  $< 3$ . Error bars correspond to  $1\sigma$  confidence intervals for average or median values based on a Bootstrap analysis. The panels include the results from the Kendall-Tau correlation test: the correlation coefficients  $r_\tau$  and their corresponding  $p$ -value (the probability of no correlation). The panels of absorption lines with detections in only two subsamples also show the results from Student’s  $t$ -test: the difference between a pair of mean values given by the  $t$  coefficient and their corresponding  $p$ -value (the probability of significant difference amongst means).

while high-ionization gas seen in absorption arises in multiple, extended structures spread over  $\sim 100$  kpc (??)

#### 4.4. CII/CIV line ratio

A further inspection of the differences between LIS and HIS on the different galaxy parameters come from the CII/CIV equivalent width line ratio. We focus on Carbon ions as they provide stronger absorptions with higher S/N compared to aluminium or silicate ones. Figure 8 shows CII/CIV line ratio as a function of impact parameter, stellar mass, and star formation rate. CII/CIV line ratio appears to anticorrelate with impact parameter ( $b$ ), stellar mass and star formation rate. Similarly to the analyses for individual line absorptions, we ran a Kendall-Tau to assess possible correlations for CII/CIV line ratio and included it in all panels of Figure 8. We confirm that the anticorrelations between CII/CIV ratio and impact parameter, stellar mass, and star formation rate are statistically robust. This suggests that CII is more important than CIV in the inner regions of these star-forming galaxies, while the opposite occurs in the outskirts at large separations.

On the other hand, star-forming galaxies and low-stellar mass with low-star formation rates show a higher CII/CIV line ratio compared with galaxies that have high stellar mass and high star formation rates. Our results suggest that galaxies with higher star formation rates and large stellar masses are capable to sweep out the highly ionized gas (traced by CIV) farther away from the galaxy compared with less star-forming and less mas-

sive galaxies. Another possible explanation is that more active and massive galaxies have stronger ionizing fluxes, able to ionize gas at larger distances compared with less massive and less star-forming galaxies. Recent studies have shown that fast and energetic outflows can push material away from the central regions in star-forming galaxies, more effectively in galaxies with large SFR (with a weaker dependence on stellar mass; ???). The presence of an AGN can make this effect even more dramatic, as shown by an enhanced gas budget in H I and low-ionization gas in high-redshift ( $z > 2$ ) galaxies (?), suggesting larger accretion rates or a net gain of cold gas in the CGM in these star-forming galaxies (?). However, the physical mechanism through which the AGN removes and/or heats the gas and suppresses accretion is not clear (?). Determining the nature of the source responsible for ionizing the gas in the CGM is crucial to improve our understanding of the multi-phase CGM, but is beyond the scope of this paper.

#### 4.5. Ly $\alpha$ -emission

As we already noted in section 4.1 (Figure 5), the Ly $\alpha$  emission component is clearly detected in our composite spectra. Figure 9 shows the Ly $\alpha_{\text{em}}$  rest equivalent width as a function of the impact parameter. We find that Ly $\alpha_{\text{em}}$  decreases as a function of the impact parameter  $b$  similarly to what ? reported from 2D Ly $\alpha_{\text{em}}$  maps. We also explore the Ly $\alpha_{\text{em}}$  equivalent width strength as a function of the galaxy stellar mass, star formation rate and azimuthal angle. However, we do not find any significant correla-

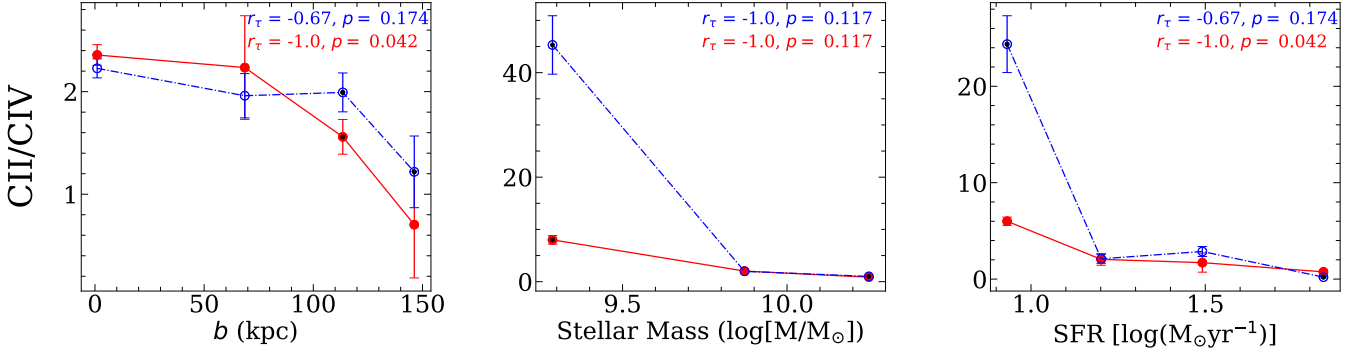


Fig. 8:  $C_{II}/C_{IV}$   $W_0$  line ratio as a function of the impact parameter  $b$ , and the *foreground* galaxy's stellar mass and SFR.  $C_{II}/C_{IV}$   $W_0$  were obtained considering the exact same set of *fg-bg* galaxy pairs. Average and median  $W_0$  are shown in solid-red and open-blue symbols, solid black symbols correspond to upper limits with  $SNR < 3$ . Error bars correspond to  $1\sigma$  confidence intervals for average or median values based on a Bootstrap analysis.

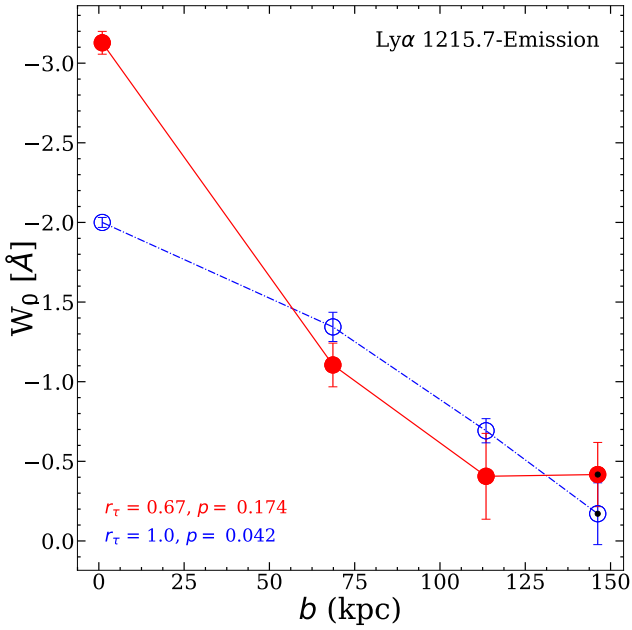


Fig. 9: Equivalent width ( $W_0$ ) for the  $Ly\alpha$  emission as a function of the impact parameter ( $b$ ) obtained from the average (solid red-line) and median (dot-dashed blue-line) composite spectra. Error bars correspond to  $1\sigma$  CIs for average or median values based on a Bootstrap analysis.

tion in these cases. This might be caused by the fact that at  $z \sim 2$  the  $Ly\alpha_{em}$ -stellar mass relation is weaker compared with galaxies at higher redshifts (?). Another possibility is the fact that our  $Ly\alpha_{em}$  measurements come from composite spectra, hence coming from star-forming galaxies with and without direct  $Ly\alpha_{em}$  detections ( $EW \leq 0\text{\AA}$ ,  $EW > 0\text{\AA}$  and  $EW \geq 20\text{\AA}$  ??), covering a wide range of stellar masses and star formation rates that may have diluted a real  $Ly\alpha_{em}$  signal (?).

## 5. Discussion

Analyses of low and high-ionization state absorption features and their dependence on stellar mass, star formation rate, and galaxy inclination have been widely explored at  $z \lesssim 0.5$  (see ??). At high-redshift however, the studies of the CGM are limited.

? used 512 close ( $< 15'' = 124\text{kpc}$ ) angular pairs of  $z \sim 2-3$  ( $z_{bg} \sim 2.3$ ) galaxies to map the cool and diffuse gas around galaxies. They found strong evidence suggesting the presence of superwind outflows and proposed a simple model of the gas in the CGM, where cool gas is distributed symmetrically around every galaxy, accelerating radially outwards with the outflow velocity increasing with radius. Later, ? and ? reported detections that suggest that in galaxies at  $\langle z \rangle = 2.4$  the CGM extends at least up to 180 kpc. Moreover, the mass of metals found within the halo is substantial and equivalent to  $\sim 25\%$  of the metal mass within the interstellar medium (?). This is, however, a lower percentage than what has been reported from studies in low-redshift galaxies (?), that suggests a considerable redistribution of the metal content of galaxies in an inside-out fashion over the last  $\sim 8.5$  Gyr. We note that eight of the nine resonance  $Si\ II$  transitions fall within the  $[900-1900]\text{\AA}$  wavelength range considered here:  $\lambda 989$ ,  $\lambda 1020$ ,  $\lambda 1190 - 1193$ ,  $\lambda 1260$ ,  $\lambda 1304$ ,  $\lambda 1526$ , and  $\lambda 1808\text{\AA}$  (?). Lines located blueward to  $Ly\alpha$  are not included in our analyses, as the result of the low coverage of our composite spectra at this wavelength range and because UV continuum level blueward to  $Ly\alpha$  is particularly sensitive to the dust content, metallicity, and the age of the stellar population (?) and their strength could be affected by IGM absorptions (?). The  $\lambda 1304$  component is blended with  $O\ I\ \lambda 1302$  absorption line and is close to excited fine-structure emission transitions that could lower  $W_0$  measurements (?). Finally,  $\lambda 1526$  is the least resonance component affected by blends (?) and is the strongest  $Si\ II$  line amongst their counterparts. In this work, we chose  $\lambda 1526\text{\AA}$  for our  $Si\ II$   $W_0$  computations as this component is free of blending effects caused by the low spectral resolution of our dataset. However, as noted by ?  $Si\ II$  transitions probe diverse optical depths, and hence the most accurate way to compute  $Si\ II$  absorption strength is to consider the contributions of all the  $Si\ II$  resonance components ( $\lambda\lambda 1260, 1304, 1526\text{\AA}$ ) within the analysed range, by averaging their strengths and deblending them from nearby spectral features that could affect their individual  $W_0$  measurements. Nevertheless, different studies have adopted diverse strategies to compute the LIS (including  $Si\ II$  resonance components)  $W_0$  strength. For example, ? averaged  $Si\ II$   $\lambda\lambda 1260, 1304, 1526\text{\AA}$ ,  $O\ I\ \lambda 1302$ ,  $C\ II\ \lambda 1334$ ,  $Al\ II\ \lambda 1670$ ,  $Fe\ II\ \lambda 2382$  and  $Mg\ II\ \lambda\lambda 2796 - 2803$  components, ? considered the average of the eight  $Si\ II$  resonance components to estimate the  $W_0$   $Si\ II$  absorption in high- $z$  Damped Lyman  $\alpha$  (DLA) systems, ? averaged  $\lambda 1526$ ,  $Si\ II$ ,  $Al\ II\ \lambda 1670$ ,  $Ni\ II\ \lambda\lambda 1741 - 1751$ ,  $Si\ II$

$\lambda 1808$ , and  $\text{Fe II } \lambda 2382\text{\AA}$  absorption lines to compute an overall LIS average absorption estimation, while later on ? considered  $\lambda 1260$ ,  $\text{O I-Si II } \lambda \lambda 1302 - 1304$ ,  $\text{C II } \lambda 1334$ , and  $\text{Si II } \lambda 1526\text{\AA}$ , for similar computations. The differences in the number of Si II resonance components considered for  $W_0$  computations could be the reason why similar Si II trends as those of C II with SFR and stellar mass shown in Fig. 7 are not appreciated. As shown by ? different low-ions transitions (Si II, Fe II, and Ni II) show non-uniform covering fractions in the CGM of star-forming galaxies at high redshift ( $z \approx 2 - 3$ ).

In this work we have used a sample of 238 galaxy close pairs to probe the CGM around star-forming galaxies at  $z \sim 2.6$ . Our results show an anticorrelation between the equivalent width of the absorption lines and the impact parameter ( $b$ ) for this high redshift star-forming galaxy sample and are consistent with previous results at lower redshift. Here we detect  $\text{Ly}\alpha/\text{LIS}$  and HIS absorption at distances up to 172 kpc and 146 kpc. Our low-ionization state (C II, Si II), and high-ionization state (C IV Si IV) absorption lines detections shape an upper envelope of the equivalent width distribution coming from studies at low redshift (see Figure 6). This is further illustrated by the differences in the slopes of the  $W_0$  radial profiles between low- and high-ionization state absorptions of the same ion species, where Si II–Si IV and C II–C IV absorption line pairs are different at  $\geq 5\sigma$  level. Moreover, when compared with galaxies at  $z \sim 2.3$  (?) our results show a significant difference in their slopes at a  $5\sigma$  level for Si II and  $3\sigma$  level for C II and Al II absorption lines. These discrepancies between LIS and HIS suggest that, within the CGM, cold ( $T < 10^{4.5}\text{K}$ ) and dense gas is more extended in galaxies at  $z \sim 2.6$  compared with galaxies at  $z \sim 2.3$  and lower redshifts, as probed by Si II, C II, Si IV C IV. These results suggests a potential redshift evolution for the CGM gas content that produce these absorptions. As higher covering factors of neutral gas lead to stronger absorption lines (?), this suggests a higher content of neutral gas in high redshift galaxies compared with low-redshift galaxies. This concentration of neutral gas could represent a reservoir of gas that can be later accreted onto the galaxies to fuel future star formation (??).

We note that it is possible to increase the maximum angular projected separation ( $\geq 23''$ ) allowing us to probe larger distances closer to the CGM and IGM boundary following ?. However, we have limited our analyses to  $23'' \sim 170\text{kpc}$  and galaxy spectra with highly reliable redshifts to guarantee detection with good S/N. Spectra with unreliable redshift measurements could wash out the expected metal absorptions and/or produce spurious features in the final composite spectra. This is further supported by the observed metallicity dependence with impact parameter, where LIS are preferably located in the inner CGM (close to the galaxy; ?) while HIS (e.g. O VI are expected to dominate the CGM at larger separations ?) making it difficult to detect weak LIS absorptions at larger separations given their expected  $W_0$ .

### 5.1. LIS/HIS absorption dependencies.

At  $z \leq 1$ , ? explored a sample of 45 Mg II absorption systems in high-resolution QSO spectra, and studied their spectra, together with the C IV and Fe II absorption profiles, suggesting that the gas responsible for Mg II and C IV absorptions arises from gas in different phases, (i.e. gas producing HIS absorption features have typical temperatures  $T > 10^5\text{K}$  ?). Moreover, they observed an evolution of the absorbing gas, that is consistent with scenarios of galaxy evolution in which mergers and accretion of "protogalactic clumps" provide gas reservoirs responsible for the

elevated star formation activity at high-redshift, while at intermediate and lower redshifts ( $z \leq 1$ ), the balance of high- and low-ionization state CGM gas may be related to the presence of star-forming regions in the host galaxy (?). Later on, ? found that early-type (quiescent, red) galaxies ( $0.37 < z < 1$ ) are associated with weaker Mg II absorptions while stronger systems are located in late-type (star-forming, blue) galaxies. These results provided evidence that the SFR correlates with Mg II absorption strength caused by the presence of outflows from star-forming/bursting galaxies. This scenario is also supported by subsequent studies that demonstrated that SFR correlates with outflow velocity deduced from the Mg II absorption strength (????), and by the correlation between the stellar mass and  $\text{Ly}\alpha$  absorption strength (??).

Our detection of LIS and HIS absorption lines suggests that at  $\langle z \rangle \sim 2.6$  C II and C IV features are correlated with star formation rate and stellar mass. C II is stronger in galaxies with low star formation rates and low stellar masses, while C IV is stronger in galaxies with high SFR and large stellar masses. These results are consistent with what has been reported for low-redshift galaxies in scenarios where LIS and HIS absorbers have different spatial distributions. Low-ionization state metal absorbers probe the gas that is less ionized than high-ionization state metal absorbers (?) and thus they are expected to be located in gas regions with different density conditions (?). Moreover, studies of low-redshift galaxies ( $z \leq 0.5$ ) have shown that as a consequence of the interaction between a starburst-driven wind and the pre-existing CGM at radii as large as 200 kpc, the CGM around star-forming galaxies with high star formation rates differs systematically compared to galaxies with lower SFRs, as probed by  $\text{Ly}\alpha$ , Mg II, Si II, C IV, and O VI absorption lines (????). However, as suggested by ? and ?, their correlation with stellar mass and star-formation rate in fact might be a consequence of a main-sequence offset, rather than simply a correlation with star-formation rate or stellar mass and as LIS/HIS covering factors can be affected by environmental processes (?). Hence, caution should be taken when interpreting LIS/HIS correlations with SFR and/or stellar mass.

The origin of the reservoir of cold neutral gas around low stellar mass galaxies and low SFRs at these distances ( $\langle b \rangle \approx 120\text{kpc}$  see Appendix A) is uncertain. One explanation come from a soft radiation field unable to ionize HIS (i.e. C IV, Si IV), as the production of C IV, Si IV absorption features in the CGM, requires photons with energies  $> 45\text{ eV}$  associated with hard ionizing radiation fields from massive stars, AGN, and radiative shocks ??. In fact as shown by ? HIS are more affected by high-velocity outflows, they show a strong correlation with SFR and are ubiquitous in high-SFR systems. Another possible explanation comes from the galactic fountain scenario, predicted by cosmological galaxy formation simulations (??), and where the presence of cold low-ionization gas result from metal-rich gas ejected in previous star-formation episodes that fall back to the disk (??). Moreover, we know that stellar winds are dominant in the inner region of the CGM  $< 60\text{kpc}$  (?), and depending on their velocity, stellar winds in low mass galaxies might be able to expel material or be reaccreted as recycled material (?). However, if the velocity outflow is insufficient to eject material out into the IGM, the recycle time scales in low-mass galaxies in which gas returns to the galaxy can be small as those in high-mass systems (?). In fact, ? detected Fe II Doppler shifts and the  $V_{\text{max}}$ -Mg II values that suggest that outflows reach the circumgalactic medium with Mg II absorption at blueshifts as high as  $700\text{ km s}^{-1}$ , reaching 70 kpc in 100 Myr, a short enough time for the host galaxy to sustain SFR even if the SFR declines due to an outflow.



Nevertheless, our measurements do not allow us to break-down the multiple components of the absorption features in our foreground galaxy ("down-the-barrel") composite spectra and detect blue-shifted offsets that could be related to high-velocity outflows. We note that it is possible to combine down-the-barrel and QSO/galaxy-galaxy pairs to unambiguously detect blue-shifted absorptions relative to the galaxy systemic velocity, and quantify independently the main properties of the detected outflow (??).

Fig 7 (lower panels) shows the dependence of line absorption strength with galaxy's effective radius ( $r_{\text{eff}}$ ) and azimuthal angle ( $\phi$ ). Concerning the dependence of the absorption strength ( $W_0$ ) with the size of the galaxy given by the effective radius ( $r_{\text{eff}}$ ), we find that LIS are stronger in smaller galaxies compared to HIS absorptions that are shown to be stronger in larger galaxies, in agreement with ? who reported that LIS absorption occurs spatially closer to the galaxy, and gas producing HIS absorptions can be located well beyond the virial radius. Regarding the dependence with azimuthal angle, we do not find any significant correlation with  $\phi$  for both LIS and HIS. However, these results are based on the fraction of galaxies for which we have morphological measurements ( $\sim 40\%$  of the parent sample). Thus, these results have to be confirmed by a similar morphological analysis using larger samples at these high redshifts, as galaxy orientation plays a major role in the measured strength of LIS and HIS. This has been shown at low-redshift from studies using down the barrel (??) and QSO-galaxy pairs (??) analyses. Moreover, at  $z \gtrsim 2$  star-forming galaxies have clumpy morphologies (?), with galactic winds that are mainly driven by outflows from prominent star-forming clumps (?), and have not formed yet a stable disk (if any) capable of collimate galactic winds into bipolar outflows (?), indicating that the minor/major axis dichotomy, associated with rotation present at low-redshift ( $z < 1$ ) is not broadly applicable at  $z \sim 2-3$  (???). Therefore, it is not obvious that at high-redshift ( $z \gtrsim 2$ ) the azimuthal angle can be determined and, if it can, it has any physical meaning.

The dependence of LIS and HIS absorption strength on the azimuthal angle has been explored in the literature to prove/disprove theories on how galaxies accrete gas from the intergalactic medium. Inflowing material along filaments in the IGM is expected to be the largest source of accretion (?). Simulations have shown that accretion of metal-poor gas inflows occurs along the major axis of galaxies, where outflows are preferably located along the semi-minor axis form bipolar outflows (?), and gas being accreted onto galaxies that later can trigger star formation has been supported from evidence collected by multiple CGM studies at low-redshift (????????????). Recent cosmological hydrodynamical simulations examine the physical properties of the gas located in the CGM of star-forming galaxies as a function of angular orientation (?). They found that the CGM varies strongly with impact parameter, stellar mass, and redshift. Moreover, they suggest that the inflow rate of gas is more substantial along the galaxy major axis, while the outflow is strongest along the minor axis.

The correlations between C II and C IV with impact parameter, star formation rate, and stellar mass scenario of a multi-phase CGM where LIS absorptions are produced by denser gas located closer to the galaxy, whether this dense neutral gas component is part of an outflow or material falling back to the galaxy taking part of a galactic fountain that eventually could be funnelled to the galaxy to sustain star formation activity (?) is not clear and can not be assessed by our datasets. On the other hand, HIS absorption features associated with strong stellar winds produced by high star formation activity capable to ionize radiation in high

stellar mass galaxies with high star formation activity sweeping out material to the outer regions of these galaxies (????).

Similar analyses including observations at different redshifts coming from different complementary surveys (e.g. VANDEL (??), zCOSMOS (??), VVDS(?), DEIMOS10K (?)), can help to increase the number of galaxy pairs with close angular separations ( $b < 6''$ ), deblend close spectral line features (e.g. C II-O IV  $\lambda\lambda$  1334.5-1343.0 Å; Si IV  $\lambda\lambda$  1393.8-1402.8 Å), and cover different low- and high-ionization state lines (e.g. O VI  $\lambda\lambda$  1032-1038 Å, Mg II  $\lambda$  2798 Å). Additionally, as it has been shown AGN activity is dependent on stellar mass and SFR (e.g. ???), thus, studies considering *bg*/QSO-AGN galaxy pairs (??) are needed to study the effect that the presence of an AGN has on feedback and quenching in star-forming galaxies at low- and high-redshifts.

## 5.2. C II / C IV line ratio.

A further inspection of the differences between LIS and HIS on the different galaxy parameters explored comes from C II/C IV line ratio. We found that C II/C IV line ratio anti-correlates with impact parameter, stellar mass, and star formation rate. This implies that C IV is mostly located at larger distances in more massive galaxies with higher star formation rates, while C II dominates at smaller impact parameters and is found mostly in low stellar mass galaxies with low star formation rates. These results further support the picture of a multi-phase CGM where LIS line absorptions are produced by denser gas with lower temperatures ( $T < 10^{4.5} \text{ K}$ ) that is located close to the central galaxy while HIS line absorptions are produced by warm gas located at larger distances from the central galaxy. Simulations have shown that much of the ongoing gas accretion occurs towards the edges of the galaxies to avoid the dominant feedback (outflows) from the central regions (???), however, we do not find supporting evidence of the low-redshift scenario where low-ionization state gas infalls along the major axis of star-forming galaxies, accompanied by large-scale outflows along the minor axis forming bipolar outflows. On the contrary, our results suggest that this scenario is not broadly applicable at  $z \sim 2$ . We note that, we have also explored Si II / Si IV and Al II / Al III equivalent width line ratios, however, we did not detect any significant correlations. On one hand, Si IV predominantly arises in denser gas closer to galaxies more similar to other LIS state lines such as Mg II than to that of higher ions (??), and hence Si II and Si IV line absorption might be probing gas with similar physical conditions. On the other, Al III is an intermediate-ionization state (IIS) tracer of moderately photoionized warm gas generally associated with neutral phase gas (???). In fact, Al III absorption is associated with low-ions as shown by the significant correlation between the velocity widths of Al III and low-ionization species (e.g. Si II, Fe II, Zn II, ?), suggesting that a substantial fraction of the low-ionization ions may be associated with moderately ionized gas traced by Al III, Fe III (?) and that, doubly ionized species (e.g. Al III, Fe III, C III, Si III) often have comparable column densities to the singly ionized (e.g. Al II, Fe II, C II, Si II) ones (?).

## 5.3. Ly $\alpha$ -emission.

Regarding Ly $\alpha_{\text{em}}$ , several studies have been carried out to explore the relation with galaxy properties. At low-redshift ?, used the Lyman Alpha Reference Sample (LARS) to obtain correlations between Ly $\alpha$  and different galaxy properties (i.e. star formation rate, dust extinction, compactness, and the gas covering

fraction). At high-redshift it has been found that bluer galaxies show stronger  $\text{Ly}\alpha_{\text{em}}$  (????), and that low-stellar mass galaxies with lower SFRs show stronger  $\text{Ly}\alpha_{\text{em}}$  than high-stellar mass galaxies with higher SFRs (???????). Additionally  $\text{Ly}\alpha_{\text{em}}$  is correlated with LIS absorption: stronger LIS absorptions correspond to weaker  $\text{Ly}\alpha_{\text{em}}$ , as high concentrations of neutral gas responsible for strong LIS absorption are also responsible for scattering out of the l.o.s.  $\text{Ly}\alpha$  photons (???). More recently ?, (?) and ? studied the spectroscopic properties of star-forming galaxies at  $z \sim 2\text{--}5$  through composite spectra grouped through different galaxy properties. They detected stronger  $\text{Ly}\alpha_{\text{em}}$  at higher redshift at fixed stellar mass, SFR, and UV Luminosity, and found that the LIS- $\text{Ly}\alpha_{\text{em}}$  relation is redshift independent suggesting that this is caused by the variations of the neutral gas covering fraction favoring  $\text{Ly}\alpha$  escape and production and/or dust content in the ISM and CGM. Moreover ?? shown that at high-redshift ( $3 < z < 4.6$ )  $\text{Ly}\alpha_{\text{em}}$  anticorrelations with stellar mass, star formation rate, and UV luminosity are stronger in low-stellar-mass populations explained by the rapidly increasing neutral gas fraction of the universe at higher redshifts (?).

## 6. Conclusions

This paper presents stacks of 238 background galaxy spectra to probe the CGM content and extent around star-forming galaxies at  $\langle z \rangle \sim 2.6$ . We use only spectra with highly reliable spectroscopic redshifts (95–100% probability of being correct) to identify the low-ionization state (LIS: Si II, C II) and high-ionization state (HIS: C IV, Si IV) metal absorption lines, and constrain their spatial distribution, and their dependence with stellar mass, star formation rate, azimuthal angle, and effective radius.

We summarize our main results below:

1. We detect LIS and HIS metal absorption lines in the CGM around star-forming galaxies at distances up to 172 kpc and 146 kpc. The limitations owing to the size of our sample do not allow us to follow metal lines beyond these distances. The strength of these absorptions decreases at increasing distances from the galaxy, consistently with results published in the literature. At any fixed distance from the galaxy, the strength of all absorption lines that we identify in our sample at  $z \sim 2.6$  is larger than any other measurement at lower redshift, providing evidence of a redshift evolution of the CGM gas content responsible for producing these absorptions.
2. We do not find any significant correlation between the LIS/HIS absorptions with the azimuthal angle ( $\phi$ ). This is opposed to the scenario at low-redshift where, cold gas (traced by LIS line) is infalling onto galaxies along the plane containing the disk, while the gas heated and processed by star-formation (traced by HIS lines) is outflowing perpendicularly to the plane. This can be explained by the fact that high-redshift galaxies have not formed a stable disk capable of collimating galactic winds into bipolar outflows. However, due to the small sample of close pairs with available morphological features, these trends need to be confirmed applying a similar analysis on larger samples at these high redshifts.
3. We find an anticorrelation between  $\text{Ly}\alpha_{\text{em}}$  and the impact parameter  $b$ , in agreement with previous results at high-redshift.
4. To assess the relative importance of LIS and HIS absorptions, we compute the C II/C IV equivalent width line ratio and found that it correlates with impact parameter  $b$ , stellar mass and star formation rate. C II/C IV  $W_0$  line ratio is higher at small separations, mainly detected in star-forming galaxies

( $\langle z \rangle \sim 2.6$ ) with low stellar masses and low star formation rates. Conversely, small C II/C IV line ratios are defined by stronger C IV line absorption compared to C II and observed at large separations in star-forming galaxies with higher stellar masses and star formation rates.

The results presented here provide observational evidence consistent with a scenario where star-forming galaxies at  $\langle z \rangle \sim 2.6$  possess a multi-phase CGM where LIS metal absorptions are produced by denser gas, that is more extended in these star-forming galaxies. Our results suggest that galaxies with higher star formation rates and large stellar masses have stronger ionizing fluxes, able to ionize gas at larger distances and/or are capable to sweep out the highly ionized gas (traced by C IV) farther away from the galaxy compared with less massive and less star-forming galaxies. Subsequently, star-forming galaxies with low SFR and low stellar mass show larger reservoirs of cold gas as probed by their C II, C IV and their C II/C IV equivalent width line ratio. These large reservoirs of cold gas could be funnelled into the galaxies and eventually provide the necessary fuel to sustain star formation activity. Recently, ? has demonstrated that large-scale environment modulates star-formation by regulating the way in which galaxies breathe in/out (accrete/expell) material by exchanging material within the CGM. This process is synchronized with star-formation rate events occurring within a galaxy, and is related to maxima (minima) of SFR associated with a previous decrease(increase) in the cold circumgalactic gas phase, that halts a further rise(decline), and leads to a fall (rise) of the star formation rate in later stages. Our results from C II-peaks and C IV-troughs detected in low-mass galaxies (low SFRs) and high-mass galaxies (high SFRs) could be interpreted as the snapshots of these two different stages of the complex interplay between the ISM/CGM/IGM in which galaxies exchange material. However, we emphasize that high resolution observations are required to detect outflows expelling out material or inflows accreting cold material back to the galaxy as recycled material. We highlight that although stacking increases the S/N of the background *spotlights*, allowing to detect the faint signal produced by gas in the CGM, it also smears out the information about the spatial, kinematic and ionization properties of the CGM. Thus we reiterate the necessity to perform deeper observations with higher resolutions at this and higher redshift of multiple LIS and HIS metal lines to provide better constraints on the properties of the multiphase CGM. It is very likely that future and ongoing observations from large and deep spectroscopic surveys such as VANDELS (??), zCOSMOS (??), VVDS(?) or DEIMOS10K (?) and Integral Field Unit observations from MUSE/KMOS/JWST will help us understand more about the multiphase nature of the CGM. Future work should point towards a resolved view of the velocity field of the in-falling/out-flowing gas of galaxies at redshift  $z > 2$ .

*Acknowledgements.* We thank an anonymous referee for constructive comments and suggestions that improved the manuscript. Based on data obtained with the European Southern Observatory Very Large Telescope, Paranal, Chile, under Large Programs 175.A-0839, 177.A-0837, and 185.A-0791. This work is based on data products made available at the CESAM data center, Laboratoire d'Astrophysique de Marseille. This work partly uses observations obtained with MegaPrime/MegaCam, a joint project of CFHT and CEA/DAPNIA, at the Canada-France-Hawaii Telescope (CFHT) which is operated by the National Research Council (NRC) of Canada, the Institut National des Sciences de l'Univers of the Centre National de la Recherche Scientifique (CNRS) of France, and the University of Hawaii. This work is based in part on data products produced at TERAPIX and the Canadian Astronomy Data Centre as part of the Canada-France-Hawaii Telescope Legacy Survey, a collaborative project of NRC and CNRS. HMH acknowledge partial support from National Fund for Scientific and Technological Research of Chile (Fondecyt) through grants no. 1171710 & 1150216. E.I. acknowledges partial support from FONDE-

CYT through grant N° 1171710. MA acknowledges support from FONDECYT grant 1211951, "ANID+PCI+INSTITUTO MAX PLANCK DE ASTRONOMIA MPG 190030" and "ANID+PCI+REDES 190194". RA acknowledges support from ANID FONDECYT Regular Grant 1202007. We thank ESO staff for their support for the VUDS survey, particularly the Paranal staff conducting the observations and Marina Rejkuba and the ESO user support group in Garching. This research used Astropy,<sup>6</sup> a community-developed core Python package for Astronomy (??), Numpy (?), Scipy (?) and Matplotlib (?)

---

<sup>6</sup> <http://www.astropy.org>

## Appendix A: Supplementary tables.

Table A.1: *Foreground-background (fg-bg) galaxy pair statistics according to their stellar mass ( $\log[M_{\star}/M_{\odot}]$ ).*

ID c1	N c2	$\langle \log[M_{\star}/M_{\odot}] \rangle$ c3	$\langle b \rangle$ (kpc) c4	$\langle z_{fg} \rangle$ c5	$\langle z_{bg} \rangle$ c6
ALL	238	$9.73 \pm 0.40$	125.05	2.60	3.04
S1	61	$9.26 \pm 0.18$	125.12	2.48	2.87
S2	63	$9.60 \pm 0.07$	119.63	2.65	3.10
S3	65	$9.87 \pm 0.09$	130.42	2.58	3.04
S4	49	$10.31 \pm 0.24$	124.83	2.71	3.19

**Notes.** Column 1: Sample ID; Column 2: number of galaxies per sample; Column 3: mean stellar mass; Column 4: mean impact parameter in kpc; Column 5: mean redshift of the *foreground* galaxies sample, and Column 6: mean redshift of the *background* galaxies sample.

Table A.2: *Foreground-background (fg-bg) galaxy pair statistics according to their star formation rate ( $\log[(M_{\odot}\text{yr}^{-1})]$ ).*

ID c1	N c2	$\langle \log[\text{SFR}/(M_{\odot}\text{yr}^{-1})] \rangle$ c3	$\langle b \rangle$ (kpc) c4	$\langle z_{fg} \rangle$ c5	$\langle z_{bg} \rangle$ c6
ALL	238	$1.37 \pm 0.39$	125.10	2.60	3.04
S1	60	$0.91 \pm 0.39$	117.92	2.56	2.98
S2	62	$1.21 \pm 0.06$	128.63	2.64	3.08
S3	59	$1.49 \pm 0.09$	124.50	2.54	3.02
S4	59	$1.92 \pm 0.20$	129.21	2.67	3.08

**Notes.** Column 1: Sample ID; Column 2: number of galaxies per sample; Column 3: mean star formation rate ( $\log[\text{SFR}/(M_{\odot}\text{yr}^{-1})]$ ); Column 4: mean impact parameter in kpc; Column 5: mean redshift of the *foreground* galaxies sample, and Column 6: mean redshift of the *background* galaxies sample.

Table A.3: *Foreground-background (fg-bg) galaxy pair statistics according to their azimuthal angle ( $\phi$ ).*

ID c1	N c2	$\langle \phi \rangle$ ( $^{\circ}$ ) c3	$\langle b \rangle$ (kpc) c4	$\langle z_{fg} \rangle$ c5	$\langle z_{bg} \rangle$ c6
ALL	97	$31.34 \pm 18.12$	121.54	2.65	3.08
S1	60	$16.90 \pm 6.20$	107.74	2.69	3.15
S2	62	$44.92 \pm 6.74$	132.53	2.55	2.92
S3	59	$75.13 \pm 9.10$	118.75	2.70	3.16

**Notes.** Column 1: Sample ID; Column 2: number of galaxies per sample; Column 3: mean azimuthal angle ( $\phi^{\circ}$ ); Column 4: mean impact parameter in kpc; Column 5: mean redshift of the *foreground* galaxies sample, and Column 6: mean redshift of the *background* galaxies sample.

Table A.4: *Foreground-background (fg-bg) galaxy pair statistics according to their effective radius ( $r_{\text{eff}}$  kpc).*

ID c1	N c2	$\langle r_{\text{eff}} \rangle$ (kpc) c3	$\langle b \rangle$ (kpc) c4	$\langle z_{fg} \rangle$ c5	$\langle z_{bg} \rangle$ c6
ALL	97	$8.94 \pm 0.49$	121.54	2.65	3.08
S1	31	$2.70 \pm 0.98$	125.92	2.67	3.16
S2	33	$6.87 \pm 1.40$	120.75	2.63	3.02
S3	33	$16.88 \pm 7.39$	118.19	2.66	3.07

**Notes.** Column 1: Sample ID; Column 2: number of galaxies per sample; Column 3: mean effective radius ( $r_{\text{eff}}$  kpc); Column 4: mean impact parameter in kpc; Column 5: mean redshift of the *foreground* galaxies sample, and Column 6: mean redshift of the *background* galaxies sample.